

Technical Note

Determination of Regional Pulmonary Parenchymal Strain During Normal Respiration Using Spin Inversion Tagged Magnetization MRI

Vitaly J. Napadow,^{1*} Vu Mai,² Alex Bankier,² Richard J. Gilbert,¹ Robert Edelman,² and Qun Chen²

In clinical practice, the assessment of lung mechanics is limited to a global physiological evaluation, which measures, in the aggregate, the contributions of the pulmonary parenchyma, pleura, and chest wall. In this study, we used an MR imaging methodology which applies two-dimensional bands of inverted magnetization directly onto the pulmonary parenchyma, thus allowing for the quantification of local pulmonary tissue deformation, or strain, throughout inhalation. Our results showed that the magnitude of strain was maximal at the base and apex of the lung, but was curtailed at the hilum, the anatomical site of the poorly mobile bronchial and vascular insertions. In-plane shear strain mapping showed mostly positive shear strain, predominant at the apex throughout inhalation, and increasing with expanding lung volume. Anisotropy mapping showed that superior-inferior axial strain was greater than medial-lateral axial strain at the apex and base, while the opposite was true for the middle lung field. This study demonstrates that localized pulmonary deformation can be measured in vivo with tagging MRI, and quantified by applying finite strain definitions from continuum mechanics. J. Magn. Reson. Imaging 2001;13:467-474. © 2001 Wiley-Liss, Inc.

Index terms: lung; lung magnetic resonance imaging; lung biomechanics; tagged magnetization; strain mapping

THE ASSESSMENT OF pulmonary parenchymal mechanics is important for the diagnosis of multiple diseases in which ventilatory function is impaired. Notwithstanding, current clinical tests do not discriminate between the contributions from the pulmonary parenchyma, pleura, and chest wall to thoracic compliance, nor do they account for regional mechanical differences within the parenchymal tissue itself.

Present techniques for imaging the lungs are mostly static, such as chest radiography, high resolution computed tomography (CT) (1-3) and MRI (4-9). Although MRI holds great promise for evaluating dynamic pulmonary function (4), this modality is still challenged by limited signal to noise ratio (SNR) from low proton density, as well as image degradation from physiological motion (cardiac pulsation, respiration) and susceptibility artifacts. Several recent advances in MRI methodology, which may improve pulmonary imaging, include the use of short echo times, ultrafast spin-echo acquisitions, projection reconstruction techniques, breath-hold imaging, ECG triggering, contrast agents (perfusion imaging, aerosols), hyper-polarized noble gas imaging, and oxygen enhancement. The successful visualization of the pulmonary parenchyma by MRI should provide a basis for the ultimate development of tools to assess tissue deformation.

Owing to the difficulties associated with pulmonary imaging, the assessment of parenchymal deformation has been limited to tracking structures in proximity to the lung, such the chest wall and diaphragm (10), or by the fluoroscopic study of the motion of implanted metal beads (11,12). The metal bead technique is capable of quantifying parenchymal expansion; however, its invasive nature limits this technique to animal models. Furthermore, the coverage of this technique is limited to a region 15-25 cm³ in size. On the other hand, the application of tagged magnetization MRI (a MR method in which orthogonal bands of inverted magnetization are first applied to the tissue, and then tracked during deformation) directly to the pulmonary parenchyma may allow for explicit non-invasive quantification of local tissue deformation, or strain, within the *entire* lung. Tagging MRI has been utilized for strain mapping deforming tissue of various composition and anatomical location. Many groups have investigated cardiac muscle (13,14), while some have studied skeletal muscle, such as the tongue (15,16). However, as previously mentioned, quantifying deformation within the lung parenchyma itself has been an elusive proposal owing to the difficulty of imaging aerated tissue. In addition, imposing tagging methodologies, with adequate temporal stability to derive physiologically relevant data, has

¹Department of Mechanical Engineering, Massachusetts Institute of Technology, Cambridge, Massachusetts.

²Department of Radiology, Beth Israel Deaconess Medical Center, Boston, Massachusetts.

Contract grant sponsor: AHA; Contract grant sponsor: NIH; Contract grant number: HL57437.

*Address reprint requests to: V.J.N., 3-355a, Department of Mechanical Engineering, Massachusetts Institute of Technology, 77 Massachusetts Avenue, Cambridge, MA 02138. E-mail: vitaly@mit.edu

Received June 15, 2000; Accepted October 24, 2000.

complicated the application of this technology to the lung parenchyma.

In the present study, we used spin inversion tagged magnetization MRI to successfully quantify localized deformation within the pulmonary parenchyma during the normal respiratory cycle. We propose that this technique could have future utility in evaluating regional differences of pulmonary mechanical function in normal as well as compromised lung tissue.

METHODS

MRI experiments were conducted on 11 healthy volunteers (6 women and 5 men, ages 25–49; mean age = 35.6) using a 1.5-T MRI scanner (Magnetom VISION, Siemens AG). The MRI tagging pulse sequence was based on a fast FLASH sequence developed in our laboratory which utilizes TR = 1.65 msec and TE = 0.4 msec. The short TE, crucial for the visualization of lung parenchyma, was achieved with a 180 msec Gaussian radiofrequency (RF)-pulse and an asymmetric read-out. A rectangular field of view (FOV) was used to reduce data acquisition time. A matrix size of 80–112 × 128 was used, resulting in a total acquisition time of 132–185 msec for each image. Other imaging parameters were as follows: flip angle = 4 degrees; bandwidth = 976 Hz/pixel; FOV = 450–500 mm; section thickness = 10–12 mm. The imaging pulse sequence was preceded by 180° RF sinc inversion tagging pulses (one for each tag) of 5-msec duration, which served to saturate the longitudinal magnetization of the affected tissue forming an inversion recovery (IR)-grid. A gradient strength of 8–10 mT/m was used with each of the individual inversion pulses to create thin tagging stripes. Since the relative brightness of a pixel (in a proton density weighted image) is due principally to the amount of longitudinal magnetization just prior to the imaging pulse sequence, tissue affected by the tagging pulses appeared dark in contrast to the surrounding tissue. Contrast then decayed with time constant T1 (of parenchymal tissue).

The application of the tagging grid was performed with the subject at rest, at full exhalation, after which, upon hearing the initiation of the tagging pulses, the subject was asked to inhale deeply. Subsequent parenchymal deformation was tracked with five to six images per inhalation that showed the tagging mesh in various states of deformation. While it would be preferable to track parenchymal deformation throughout the entire pulmonary cycle, tag decay and through plane motion limits the temporal window for which adequate tag quality persists. Adequate tag quality (i.e., wherein a deformed mesh could be digitized) was, in this iteration of the project, a subjective (though conservative) decision by the software operator as to whether or not tagged tissue could be confidently distinguished from the surrounding untagged tissue.

The imaging slice (which was chosen to be either coronal, showing both lungs, or sagittal, showing the right lung) was obtained orthogonal to the tagging planes. Consequently, in a two-dimensional image of undeformed tissue, magnetic tags appeared as a square rectilinear grid (tag spacing was 25 mm). Deformation

of tagging grid elements represented actual tissue deformation and was quantified by calculating strain, a unitless measure of localized deformation independent of rigid body translation or rotation. Our methodology has been previously described in greater detail (15).

Strain in each triangular element of the two-dimensional imaging plane was assumed to be non-linear and derived by the application of Green's strain tensor transformations:

$$\mathbf{E}_{\text{Green}} = \frac{1}{2} (\mathbf{U}^2 - \mathbf{I}) \quad (1.0)$$

Where \mathbf{U} is the right stretch tensor and \mathbf{I} the identity tensor. In order to resolve the idealized material continuum of the lung, discrete triangular deforming elements were defined by digitizing nodes at tag line intersections. Thus, each triangular element was composed of two independently deforming line elements (i.e., three nodes); one along the x-axis and the other along the y-axis in the rest configuration. Each line element had length s at rest, defined by the tag spacing. Axial strains were calculated based on the lengths of the deformed line elements (s_1 and s_2 , respectively), while shear strain was calculated based on line element lengths, as well as the relative angle between adjacent line elements ($90^\circ - \phi$):

$$E_{xx} = \frac{1}{2} \left(\frac{s_1^2}{s^2} - 1 \right) \quad (2.0)$$

$$E_{yy} = \frac{1}{2} \left(\frac{s_2^2}{s^2} - 1 \right) \quad (3.0)$$

$$E_{xy} = \frac{s_1 s_2}{2s^2} \sin \phi \quad (4.0)$$

Hence, the entire two-dimensional strain tensor, \mathbf{E} , was calculated from the digitization of the tagged image.

$$\mathbf{E} = \begin{bmatrix} E_{xx} & E_{xy} \\ E_{yx} & E_{yy} \end{bmatrix} \quad (5.0)$$

Strain maps of the in-plane trace of the strain tensor were smoothed with bicubic spline surfaces and displayed by magnitude sensitive color code overlaying the original tagged images. The trace of the strain tensor, $\text{tr}(\mathbf{E}) = E_{xx} + E_{yy}$, is one of the three invariants (insensitivity to coordinate reference frame) of the strain matrix and can be considered a generalized direction-independent strain magnitude. The images were then compiled into a dynamic strain map movie, which tracked regional deformation during inhalation. Other parameters that were similarly mapped included shear strain, and the coordinate anisotropy index, $E_{yy} - E_{xx}$ (y-direction axial strain - x-direction axial strain).

The entire strain tensor was alternately represented by a spatial array of rhombi, with each rhombus centered on a tagging element's centroid. The major and minor axes of these rhombi were oriented according to the directions of the eigenvectors, and scaled to the linear directional axial stretch measured in the given

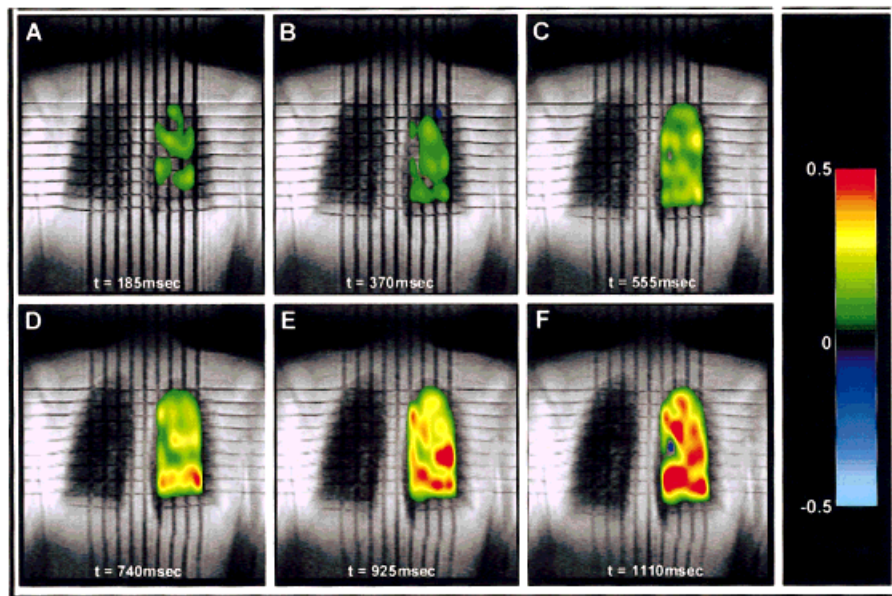


Figure 1. Coronal view of the lungs during inspiration with strain tensor trace quantification of the left lung shown. Successive images were digitized at $t = 185$ msec apart, with the last viable image acquired at $t = 1110$ msec after onset of inhalation. Strain trace mapping showed increasing strain as the lung was inflated with air. Strain trace was maximal at the base (peaking at 0.63 at $t = 1110$ msec) and was diminished at the hilus (peaking at -0.16 at $t = 1110$ msec), the location of the relatively non-distensible bronchial insertion. [Color figure can be viewed in the online issue, which is available at www.interscience.wiley.com]

tagging element (note: the major axis corresponds to the eigenvector associated with the greater of the two eigenvalues). In addition, the relative size of a rhombus was based on a scaling factor, f , which (for visualization purposes) allows icon size to be related directly to strain magnitude. The factor, f , was defined by a function of the strain tensor's independent eigenvalues (λ_1, λ_2):

$$f = \sqrt{\lambda_1^2 + \lambda_2^2} \quad (6.0)$$

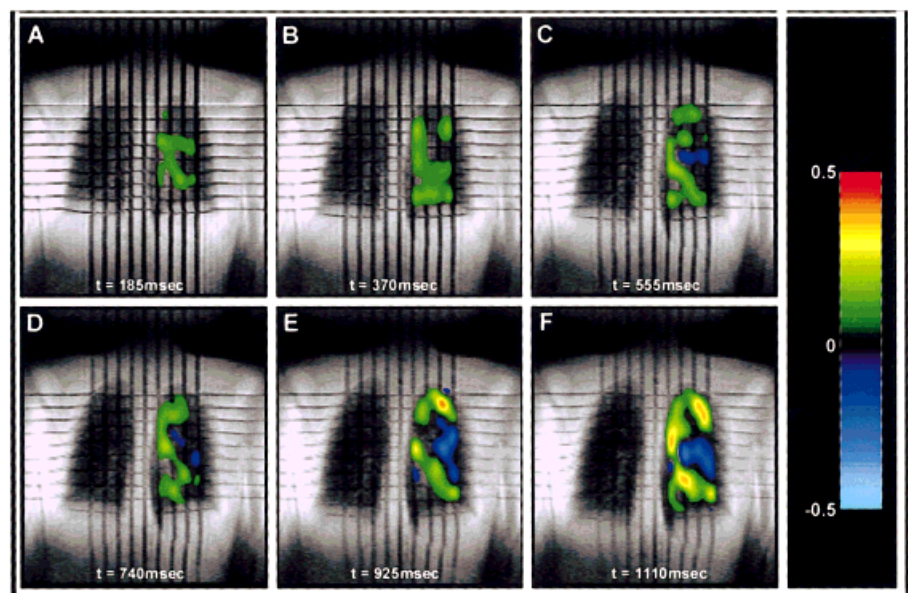
RESULTS

Strain analysis of the deformed tagging grids, acquired during normal inspiration, presented a quantifiable pattern of deformation for the lung parenchyma, displayed here for one representative subject. In most instances, one lung on the coronal view images was dig-

itized while the other was left unscathed in order to provide an adequate temporal assessment of tag definition and degree of fade. The coronal view strain maps showed a regionally variant strain field during inspiration with strain magnitude increasing as the lungs were inflated with air. The strain tensor trace was maximal at the base and apex of the lung (peaking at 0.63 at $t = 1110$ msec), but was curtailed at the root (minimum peak at -0.16 at $t = 1110$ msec), the site of the relatively non-distensible bronchial insertion (Fig. 1).

In-plane shear strain mapping in the coronal plane showed mostly positive shear strain (peaking at 0.42) which was most predominant at the apex throughout inhalation, and increased with expanding lung volume (Fig. 2). Later time points confirmed the existence of negative shear strain (peaking at -0.20) at the middle and lower lung fields.

Figure 2. Coronal view of the lungs during inspiration with in-plane shear strain mapping of the left lung shown. Successive images were digitized at $t = 185$ msec apart, with the last viable image acquired at $t = 925$ msec after onset of inhalation. Shear strain mapping showed positive shear strain (peaking at 0.42) which was most predominant at the apex throughout inhalation, and increased with expanding lung volume. Later time points confirmed the existence of negative shear strain (peaking at -0.20) at the middle and lower lung fields. Note that the polarity of shear strain is purely coordinate dependant, signifying direction of shear (see Fig. 6). [Color figure can be viewed in the online issue, which is available at www.interscience.wiley.com]



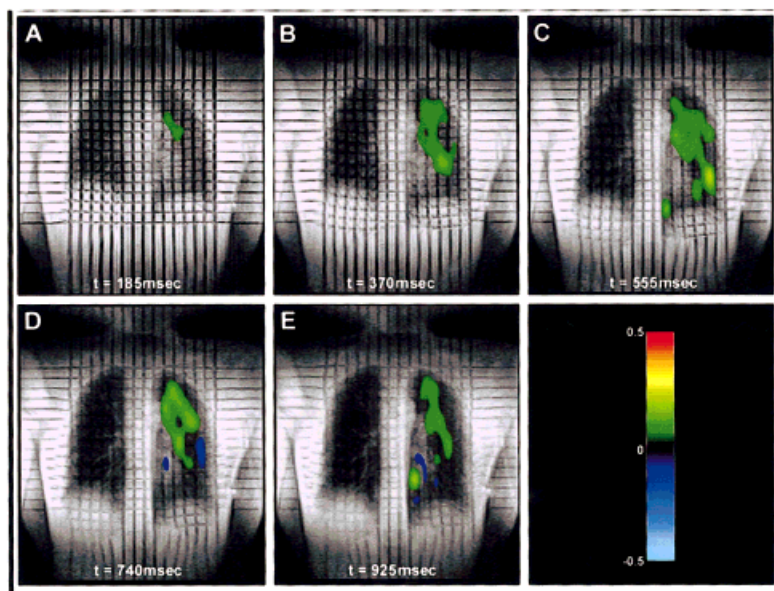


Figure 3. Coronal view of the lungs during inspiration with anisotropy ($E_{yy} - E_{xx}$) mapping of the left lung shown. Anisotropy mapping showed that y-direction axial strain was greater than x-direction axial strain at the apex and the base, while the opposite was true for the mid-lateral lung field. The difference was accentuated with time, as lung volume increased. The anisotropy index can be used to derive whether expanding regions are expanding more medial-laterally or antero-posteriorly. [Color figure can be viewed in the online issue, which is available at www.interscience.wiley.com]

Coronal plane coordinate anisotropy ($E_{yy} - E_{xx}$) mapping showed that superior-inferior directed axial strain was greater than medial-lateral directed axial strain at the apex and the base, while the opposite was true for the middle lung field (Fig. 3). Furthermore, the difference was accentuated with time, as lung volume increased.

Strain tensor visualization in coronal plane imaging showed that strain magnitude increased with expanding lung volume, with maximal axial strain being directed superior-inferior at the base and apex, and more medial-lateral toward the more lateral regions of the middle lung field (Fig. 4).

Sagittal plane imaging of the right lung with strain trace mapping showed regions of compressive strain which gradually become expanded (especially toward the apex), as more air is inhaled into the lung, peaking at 0.46 at $t = 528$ msec (Fig. 5). Maximum expansion appeared to occur at the apex of lung and was greater posteriorly than anteriorly.

DISCUSSION

While advances in pulmonary imaging have improved the visualization of parenchymal contents during static conditions, there currently exists no imaging modality to assess regional mechanics in the entire lung while the parenchyma is in motion, i.e., during inhalation or exhalation. The development of a modality with this capability should allow for the tracking of deforming tissue, the delineation of physiological variations in regional deformation, and the potential detection of areas of diminished mobility in diseased lung tissue.

In this study, we successfully evaluated respiratory mechanics through strain mapping (shear, trace, and anisotropy of the strain tensor) of the lung parenchyma by tagged magnetization MRI, and regionally variant deformation properties were discerned. The distribution of alveolar size is proportional to strain distribution within the lung, while the distribution of ventilation is

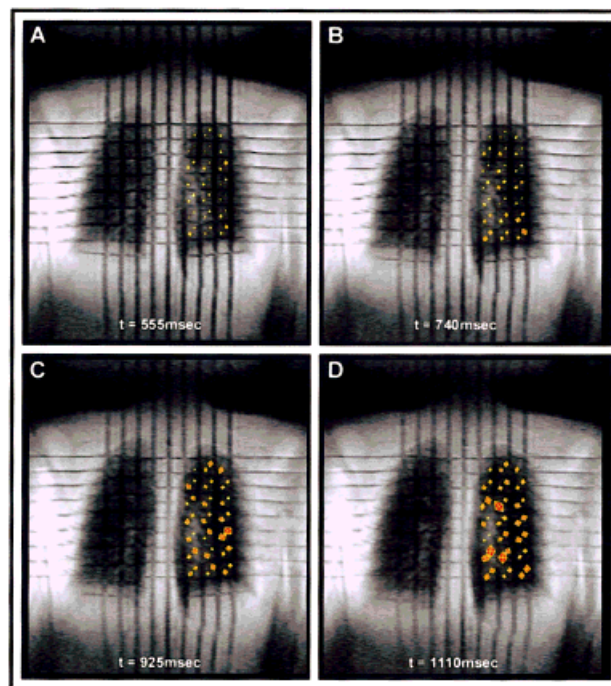


Figure 4. Coronal view of the lungs during forced inspiration with strain tensor visualization in the left lung shown. The entire strain tensor was visualized as a rhombus, whose major and minor axes were oriented along tensor eigenvectors (directions of most extreme axial strain, i.e., shear-free coordinate directions) and scaled by the magnitude of the eigenvalues. Furthermore, the entire rhombus was scaled in size by the scaling factor $f = (\lambda_1^2 + \lambda_2^2)^{1/2}$. Strain magnitude increased with expanding lung volume, with maximal axial strain being directed superior-inferior at the base and apex, and more medial-lateral toward the more lateral regions of the middle lung field. Using an icon to visualize a multi-dimensional strain field allows for the entire strain field to be visualized in one graphic. [Color figure can be viewed in the online issue, which is available at www.interscience.wiley.com]

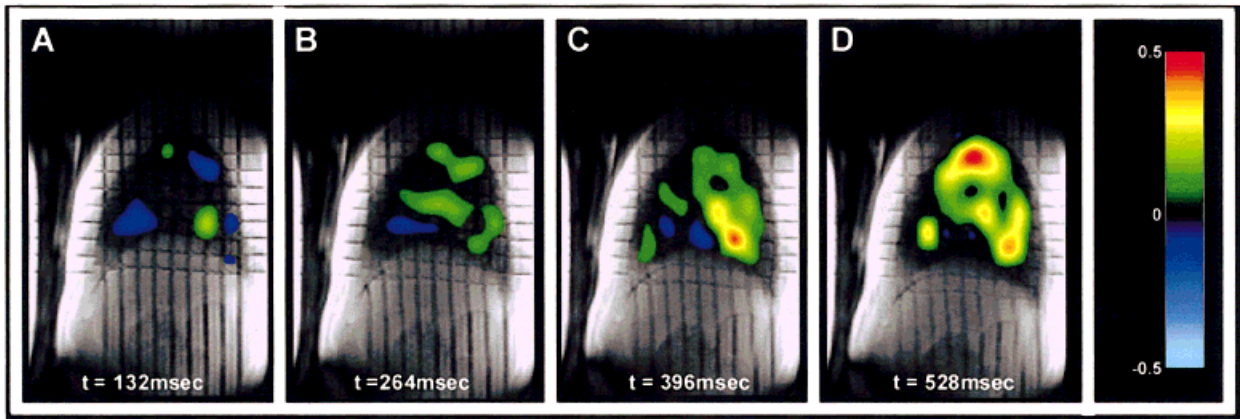


Figure 5. Sagittal view of the lungs during inspiration with strain tensor trace quantification of the right lung shown. Successive images were digitized at $t = 132$ msec apart with the last viable image acquired at $t = 528$ msec after onset of inhalation. Strain trace mapping showed increasing strain as the lung was inflated with air (peaking at 0.46 at $t = 528$ msec). Maximum expansion occurred at the apex of lung and was greater posteriorly than anteriorly. [Color figure can be viewed in the online issue, which is available at www.interscience.wiley.com]

proportional to the change in strain (17). Hence, strain mapping of the lung parenchyma is a very relevant measure of pulmonary mechanics.

Through this analysis, several novel insights regarding respiratory mechanics were revealed. We found that the magnitude of parenchymal strain increases in all regions as the lung is inflated with air (Fig. 1). While all regions of the lung demonstrated progressively increasing deformation, the trace was maximally increased at the base and lateral portions of the lung. The base of the lung may show a higher magnitude of strain because of its close proximity to the prime inhalatory effector muscle, the inferiorly displacing diaphragm. The trace was notably diminished at the hilum, or root, of the lung, where the relatively immobile bronchial tree and vasculature insert into the lung parenchyma (best evident at $t = 1110$ msec). As the branching continues into the more distant reaches of the lung, the bronchioles become finer and finer, with diminished fibrocartilage content in the more distensible tissue. As a result, when the more distensible tissue is subjected to acinar filling, a greater magnitude of strain results.

The regionally variant properties of strain seen during inhalation could reflect the variability of ventilatory phase-specific air flow zones. Anatomic conformation may result in the preferential flow of inhaled air down one bronchial branch over another, until regional filling due to the former alters anatomic airway conformation enough to increase flow to other regions of the lung. Furthermore, it is also conceivable that the supine positioning necessary for MRI scanning influences the strain properties seen on the scan. Generally speaking, heterogeneous patterns of deformation have been predicted by many researchers (12,17), and our data corroborates qualitatively with their results. Unfortunately, there are no quantitative in vivo strain data in the literature to make an adequate comparison.

In-plane shear strain mapping of inhalation resulted in another interesting observation (Fig. 2). Shear strain was mostly positive (peaking at 0.42) and was most prominent at the apex throughout inhalation, increas-

ing with expanding lung volume. Later time points confirmed the existence of negative shear strain (peaking at -0.20) at the middle and lower lung fields. Shear measured relative to the vertical and horizontal coordinate axes signifies a relative difference in expansion or contraction of neighboring regions along those axes. In other words, shear strain connotes a change in element shape as opposed to normal strain, which connotes a change in element area; note that the polarity of shear strain is purely arbitrary, signifying direction of shear (Fig. 6). Positive shear seen in the lung most likely signifies an expansion of parenchyma in a supero-lateral direction, away from the relatively immobile hilum. In testing pathological lung tissue, such as in fibrosis or sarcoidosis, a resulting shear mapping may show increased shear strain compared to what one would expect for the amount of axial strain observed, as regions of relatively unaffected normally expanding paren-

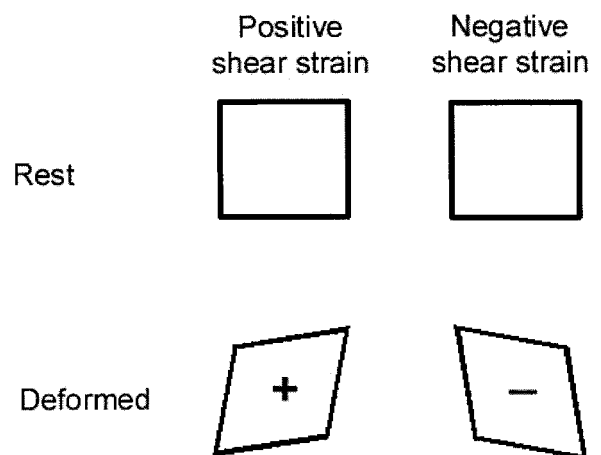


Figure 6. Shear strain, as opposed to axial strain, connotes a distortion (change of shape without change of area). Polarity of shear strain is arbitrarily assigned, signifying only the direction of angular deformation. The above figure reflects the convention adopted for our analysis of lung parenchyma strain.

chyma may exist in close proximity to regions of more immobile fibrotic parenchyma.

Anisotropy mapping of the lung during inhalation can provide data regarding preferred directions of expansion (Fig. 3). The anisotropy index was defined as the difference between superior-inferior and medial-lateral strain ($E_{yy} - E_{xx}$), hence, positive anisotropy connotes greater expansion in the superior-inferior direction than the medial-lateral, while negative anisotropy connotes the converse. Anisotropy mapping presented positive anisotropy at the apex and the base, and negative anisotropy for the mid-lateral lung field (evident at later time points). This difference was accentuated with increasing lung volume. Preferential directional expansion could be due to many factors including anatomical barriers such as the ribs, and involved muscular displacement, such as diaphragm motion. The latter effect may induce preferentially superior-inferior axial strain at the lung base, especially early in the inhalatory phase. Furthermore, positive anisotropy at the apex can be explained by the fact that the lateral excursion of the first rib is decreased when compared to its more distal neighbors, thus promoting parenchymal expansion superiorly, rather than laterally, in this region. Similarly, increased medial-lateral strain (relative to superior-inferior strain) later in the inhalation phase could signify an increase in the lateral displacement of the 4th or 5th rib edge, thus allowing more room for pleural displacement. Another explanation would simply be the increased filling of more laterally located bronchopulmonary segments, which may occur preferentially at later time points in inhalation. It should be interesting to see how various pathologies (fibrosis, neoplasm, etc.) affect the pattern of anisotropic parenchymal expansion during inhalation.

Coronal view strain tensor visualization was completed in order to visualize the entire strain tensor in one image (Fig. 4). The visualization was completed for only the last four digitized images, as tensor presentation in the first two images was insignificant. Strain magnitude increased with expanding lung volume, with maximal axial strain being directed superior-inferior at the base and apex, and more medial-lateral toward the more lateral regions of the middle lung field. Visualization of the entire strain tensor can delineate regions of similarly deforming (in orientation and magnitude) tissue and allows for the entire strain tensor to be visualized simultaneously.

Sagittal plane imaging of the strain tensor trace showed increasing strain as the lung was inflated with air, with maximum expansion occurring at the apex of the lung and increased expansion posteriorly, compared to the anterior lung fields. Regions of negative strain seen in several regions were most likely due to mistimed imaging wherein tagging was accomplished while the subject was at the very end of his expiratory phase (as opposed to being immediately before his inspiratory phase).

The tagging methodology proved to be robust in coronal plane imaging, lasting up to 1110 msec. Tags in non-lung tissue (muscle, connective tissue), which, to a large degree, does not displace through-plane during

inhalation as much as lung parenchyma, lasted up to 3000 msec after placement.

However, when the imaging slice was in the sagittal plane, the last viable image occurred at $t = 528$ msec, about half of the value for the last digitizable image in coronal plane imaging. This result was most likely due to increased parenchymal deformation medial-laterally (hence quicker tag fade) than antero-posteriorly (which would induce tag fade in with coronal plane imaging).

Despite these promising results, our technique still has several limitations. Further efforts will be focused on increasing tag retention time. Because tag fade does not permit us to track an entire breathing cycle, not only is valuable data missed from end-inhalation, but intersubject comparisons are difficult to make. The latter problem stems from the fact that it is unclear how total lung capacity (TLC) varies for different subjects, or what fraction of TLC any given image represents. In future investigations, we hope to be able to use a pre-defined imaging/spirometry calibration relationship to determine fractional TLC for any given image. This normalization technique may then make it possible to make intersubject comparisons. Another issue is that respiratory motion is a three-dimensional phenomenon, while our technique images only a single slice. Hence, through-plane deformation is difficult to track. Furthermore, through-plane motion may actually result in parenchymal tissue traveling outside of the original imaging slice (contributing to image blurring). Further developments of our technique will therefore be oriented towards a multi-slice or three-dimensional acquisition, rather than a single slice acquisition, with the ultimate goal of covering the entire volume of the lung.

We anticipate that the technique of tagged magnetization of the pulmonary parenchyma will have significant utility in assessing pulmonary function, where regional mechanical differences are likely to exist. For example, the variability of parenchymal strain patterns with subject body position could be studied. From a clinical perspective, if a given lobe or segment is restricted in its motion due to infection, tumor, fibrosis, or acute/ventilator-induced lung injury, this may impact on the ability of this segment, as well as adjacent segments, to adequately expand during inspiration. Consequently, the basis for impaired oxygenation in these patients may only become apparent when parenchymal mechanics are fully detailed. Current diagnostic approaches for evaluating such patients include (in order of increasing invasiveness) chest radiography, high resolution CT scan, bronchoscopy, and thoracoscopic lung biopsy. However, none of these modalities measures pathological tissue motion. Our technique successfully overcomes this limitation, and thereby provides the basis for a dynamic mechanical assay that could be used to follow up patients in order to monitor the effects of therapy on the mechanics of the lung parenchyma. Moreover, areas of fibrosis (or other dense matter) within the parenchyma should only serve to increase SNR, thereby improving the temporal limits to which the tags in the tissue will prove viable.

We conclude that spin inversion MRI with tagged magnetization constitutes a method to assess local pulmonary parenchymal deformation during the respira-

tory cycle. The application of this method should be advantageous for more completely characterizing and quantifying regional differences of mechanical function in health and disease.

ACKNOWLEDGMENTS

This research was partly supported by AHA (QC) grant and NIH grant HL57437 (RRE).

APPENDIX

The following is a derivation of the equations for the non-linear Green's strain tensor components.

Consider the general deforming body defined by two perpendicular line elements—one along the X (horizontal) axis, the other along the Y (vertical) axis. The deformation gradient, F , transforms any line element dX to dx :

$$dx = \mathbf{F} dX \quad (\text{A.1.0})$$

By the polar decomposition theorem, the deformation gradient can be decomposed into an orthogonal rotation tensor, R , and a symmetric, positive-definite right stretch tensor, U .

$$\mathbf{F} = \mathbf{R}\mathbf{U} \quad (\text{A.2.0})$$

Thus, assume a resting two-dimensional orthogonal Cartesian coordinate system defined by the unit vectors e_x and e_y , with:

$$\overrightarrow{AB} = se_x \quad (\text{A.3.0})$$

$$\overrightarrow{AC} = se_y \quad (\text{A.3.1})$$

while the deformed line elements can be calculated by:

$$\overrightarrow{A'B'} = \mathbf{F}\overrightarrow{AB} = s\mathbf{F}e_x \quad (\text{A.4.0})$$

$$\overrightarrow{A'C'} = \mathbf{F}\overrightarrow{AC} = s\mathbf{F}e_y \quad (\text{A.4.1})$$

Hence, since the rotation tensor does not cause any stretch, the deformed line element lengths are given by:

$$s_1 = |A'B'| = s|\mathbf{F}e_x| = s|\mathbf{U}e_x| \quad (\text{A.5.0})$$

$$s_2 = |A'C'| = s|\mathbf{F}e_y| = s|\mathbf{U}e_y| \quad (\text{A.5.1})$$

Also, the relative angle between the two deformed line elements can be given by:

$$\overrightarrow{A'B'} \cdot \overrightarrow{A'C'} = s^2 \mathbf{F}e_x \cdot \mathbf{F}e_y = s_1 s_2 \cos(\pi/2 - \phi)$$

$$s^2 \mathbf{U}e_x \cdot \mathbf{U}e_y = s_1 s_2 \sin \phi$$

$$\mathbf{U}e_x \cdot \mathbf{U}e_y = \frac{s_1 s_2}{s^2} \sin \phi \quad (\text{A.5.2})$$

The general definition of a Lagrangian strain tensor is:

$$\mathbf{E}_{\text{Lagrangian}} = \frac{1}{m} (\mathbf{U}^m - \mathbf{I}) \quad (\text{A.6.0})$$

where $m \neq 0$ is a scalar. By definition (18,19), Green's non-linear strain tensor is given by the special case, $m = 2$:

$$\mathbf{E}_{\text{Green}} = \frac{1}{2} (\mathbf{U}^2 - \mathbf{I}) \quad (\text{A.6.1})$$

Finally, the elements of this strain tensor can be derived by incorporating Eq. A.5.0–A.5.2 with the definition given in Eq. A.6.1:

$$\begin{aligned} E_{xx} &= \mathbf{E}e_x \cdot e_x = \frac{1}{2} (\mathbf{U}^2 - \mathbf{I})e_x \cdot e_x \\ &= \frac{1}{2} (\mathbf{U}^2 e_x \cdot e_x - 1) = \frac{1}{2} (\mathbf{U}e_x \cdot \mathbf{U}e_x - 1) \\ &= \frac{1}{2} (|\mathbf{U}e_x|^2 - 1) \\ &= \frac{1}{2} \left(\frac{s_1^2}{s^2} - 1 \right) \end{aligned} \quad (\text{A.7.0})$$

$$\begin{aligned} E_{yy} &= \mathbf{E}e_y \cdot e_y = \frac{1}{2} (\mathbf{U}^2 - \mathbf{I})e_y \cdot e_y \\ &= \frac{1}{2} (\mathbf{U}^2 e_y \cdot e_y - 1) = \frac{1}{2} (\mathbf{U}e_y \cdot \mathbf{U}e_y - 1) \\ &= \frac{1}{2} (|\mathbf{U}e_y|^2 - 1) \\ &= \frac{1}{2} \left(\frac{s_2^2}{s^2} - 1 \right) \end{aligned} \quad (\text{A.7.2})$$

$$\begin{aligned} E_{xy} &= \mathbf{E}e_y \cdot e_x = \frac{1}{2} (\mathbf{U}^2 - \mathbf{I})e_y \cdot e_x \\ &= \frac{1}{2} \mathbf{U}^2 e_y \cdot e_x = \frac{1}{2} \mathbf{U}e_x \cdot \mathbf{U}e_y \\ &= \frac{s_1 s_2}{2s^2} \sin \phi \end{aligned} \quad (\text{A.7.1})$$

REFERENCES

1. Lynch DA, Brasch RC, Hardy KA, Webb WR. Pediatric pulmonary disease: assessment with high-resolution ultrafast CT. *Radiology* 1990;176:243-248.

2. Olson LE, Hoffman EA. Lung volumes and distribution of regional air content determined by cine X-ray CT of pneumonectomized rabbits. *J Appl Physiol* 1994;76:1774-1785.
3. Wilcox AG. Advances in radiology for interstitial lung disease. *Curr Opin Pulm Med* 1999;5:278-283.
4. Chen Q, Levin DL, Kim D, David V, McNicholas M, Chen V, Jakob PM, Griswold MA, Goldfarb JW, Hatabu H, Edelman RR. Pulmonary disorders: ventilation-perfusion MR imaging with animal models. *Radiology* 1999;213:871-879.
5. Hatabu H, Chen Q, Stock KW, Gefter WB, Itoh H. Fast magnetic resonance imaging of the lung. *Eur J Radiol* 1999;29:114-132.
6. Kauczor HU, Kreitner KF. MRI of the pulmonary parenchyma. *Eur Radiol* 1999;9:1755-1764.
7. Maki DD, Gefter WB, Alavi A. Recent advances in pulmonary imaging. *Chest* 1999;116:1388-1402.
8. Mai VM, Knight-Scott J, Berr SS. Improved visualization of the human lung in 1H MRI using multiple inversion recovery for simultaneous suppression of signal contributions from fat and muscle. *Magn Reson Med* 1999;41:866-870.
9. Qanadli SD, Orvoen-Frija E, Lacombe P, Di Paola R, Bittoun J, Frija G. Estimation of gas and tissue lung volumes by MRI: functional approach of lung imaging. *J Comput Assist Tomogr* 1999;23:743-748.
10. Suga K, Tsukuda T, Awaya H, Takano K, Koike S, Matsunaga N, Sugi K, Esato K. Impaired respiratory mechanics in pulmonary emphysema: evaluation with dynamic breathing MRI. *J Magn Reson Imaging* 1999;10:510-520.
11. Hubmayr R, Hill M, Wilson, T. Nonuniform expansion of constricted dog lungs. *J Appl Physiol* 1999;80:522-530.
12. Hubmayr R, Walters B, Chevalier P, Rodarte J, Olson L. Topographical distribution of regional volume in anesthetized dogs. *J Appl Physiol* 1983;50:1048-1056.
13. Axel L, Dougherty L. MR imaging of motion with spatial modulation of magnetization. *Radiology* 1989;171:841-845.
14. Zerhouni EA, Parish DM, Rogers WJ, Yang A, Shapiro EP. Human heart: tagging with MR imaging—a method for noninvasive assessment of myocardial motion. *Radiology* 1988;169:59-63.
15. Napadow V, Chen Q, Wedeen V, Gilbert R. Intramural mechanics of the human tongue in association with physiological deformations. *J Biomech* 1999;32:1-12.
16. Niitsu M, Kumada M, Campeau N, Niimi S, Riederer S, Itai Y. Tongue displacement: visualization with rapid tagged magnetization-prepared MR imaging. *Radiology* 1994;191:578-580.
17. Rodarte J, Fung YC. Distribution of stresses within the lung. In: Peter T. Macklem, Jere Mead, editors. *Handbook of Physiology. The Respiratory System. Mechanics of Breathing*. Bethesda: American Physiological Society; 1986. p 233-246.
18. Chandrasekharaiiah D, Debnath L. *Continuum Mechanics*. San Diego: Academic Press, 1994. p 188-190.
19. Lai WM, Rubin D, Krempl E. *Introduction to Continuum Mechanics*. New York: Pergamon Press, 1993. p 556.